

Phase diagram of polar states in doped ferroelectric systems

Dong Wang,^{1,2} Xiaoqin Ke,^{1,3} Yunzhi Wang,^{1,3,*} Jinghui Gao,^{1,4} Yu Wang,¹ Lixue Zhang,¹ Sen Yang,¹ and Xiaobing Ren^{1,4,†}

¹Center for Computational Study of Microstructure Evolution in Materials, Multi-Disciplinary Materials Research Center, Frontier Institute of Science and Technology, State Key Laboratory for Mechanical Behavior of Materials, Xi'an Jiaotong University, Xi'an 710049, China

²State Key Laboratory for Strength and Vibration of Mechanical Structures, Xi'an Jiaotong University, Xi'an 710049, China

³Department of Materials Science and Engineering, The Ohio State University, 2041 College Road, Columbus, Ohio 43210, USA

⁴Ferroic Physics Group, National Institute for Materials Science, Tsukuba, Ibaraki 305-0047, Japan

(Received 27 September 2011; published 27 August 2012)

We report a complete phase diagram that describes the relationships among all polar states in doped ferroelectrics, including the paraelectric (polar liquid), ferroelectric (polar crystal), relaxor (polar glass), and precursory states (partially frozen nanopolar domains). We employ a model that considers a randomly distributed local polarization field associated with point defects, which breaks the symmetry of the Landau free energy with respect to polarization. In the meantime, the model also takes into account the effect of point defects on the overall stability of the ferroelectric phase. Based on this model, the phase field simulations reproduce all the polar states and important characteristics associated with ferroelectric-glass (relaxor) transition observed in experiments, including rugged free energy, wide relaxation time, nanosized ferroelectric domain structure, “diffuse” transition, temperature dependence of third-order dielectric susceptibility, nonergodicity, frequency dependence of dielectric loss, and domain switching.

DOI: [10.1103/PhysRevB.86.054120](https://doi.org/10.1103/PhysRevB.86.054120)

PACS number(s): 77.80.B–, 64.70.K–, 64.70.P–, 77.80.Jk

I. INTRODUCTION

A normal ferroelectric is characterized by a transition in polarization from a disordered state (i.e., paraelectric state or polar liquid) to a long-range-ordered state (i.e., ferroelectric state or polar crystal) upon cooling to a critical temperature called the Curie temperature T_c . The long-range-ordered state exhibits a number of important properties, such as piezoelectricity, electric switching, and pyroelectricity, making ferroelectric materials the heart of a wide range of advanced technological applications. In contrast, it has been known for decades that ferroelectric materials with complex compositions exhibit a “glassy polar state,” which is usually referred to as the relaxor ferroelectric state.^{1–6} A relaxor is neither a polar liquid nor a polar crystal but is a frozen disordered polarization state with only short-range order characterized by a “smeared” dielectric permittivity peak with frequency dispersion and nonergodicity indicated by zero-field-cooled/field-cooled (ZFC/FC) experiments.⁷ The unique frozen local ferroelectric order makes the relaxor indispensable for some key technological applications from condensers to high-power piezoelectric sensors and actuators.^{8,9}

Over the past decades, extensive efforts have been made to explore the physical origin of relaxor ferroelectrics.^{10–19} However, the long-standing question concerning the polar state in relaxors remains:^{4,19} Whether a relaxor state is in doped ferroelectrics (such as $\text{PbMg}_{1/3}\text{Nb}_{2/3}\text{O}_3$ where the presence of random fields exists), a ferroelectric state broken up into nanodomains,^{4,16} a dipolar glass state with randomly interacting polar regions,²⁰ or a spherical vector glass state with reorientable interacting random polar clusters.^{18,19} Recently, electric-field-induced domain-switching behavior at a relaxor state in an experimental observation⁴ has proved that a relaxor is essentially a ferroelectric state broken up into nanodomains under the constraint of quenched random electric fields.^{4,16} Therefore, a new model which can predict all relaxor characteristics in experiments is needed. In this paper, we propose

a model that considers two well-known effects associated with a random polarization field created by point defects in ferroelectrics: (a) a random local static polarization field that breaks the symmetry of the Landau free energy polynomial as a function of polarization^{10,11,16,17} and (b) a decrease in the normal ferroelectric transition temperature T_c of the system⁵ as defect concentration increases. Following the convention in literature,^{10,11} the former is referred to as the local field effect (LFE), whereas, the latter is referred to as the global transition temperature effect (GTTE) hereafter. Computer simulations using the phase field method based on this model have predicted all the polar states in a prototype-doped ferroelectric system and unique properties of relaxor ferroelectrics found in experiments (such as nanosized ferroelectric domain structure, “diffuse” transition, temperature dependence of third-order dielectric susceptibility, nonergodicity, frequency dependence of dielectric loss, wide relaxation time, and slim hysteresis loop). Furthermore, a complete polar state phase diagram characterizing both normal ferroelectric transition and ferroelectric-glass (relaxor) transition is established, which shows all the polar states and their relationships as functions of temperature and defect concentration.

II. MODEL

The model system considered is a generic single crystal undergoing a first-order cubic-to-tetragonal ferroelectric transition¹⁵ upon cooling. The domain structure is described by spatial distribution of spontaneous polarization $\mathbf{P} = (P_1, P_2, P_3)$. The total free energy of the system includes the following three physically distinctive terms:^{10,15,21–23}

$$\begin{aligned}
 F &= F(\mathbf{P}, \bar{\epsilon}) + F(\mathbf{P}, \varphi) + F(\mathbf{P}) \\
 &= \int_V f_{\text{bulk}} dV + \int_V f_{\text{couple}} dV \\
 &\quad + \int_V (f_{\text{elas}} + f_{\text{elec}} + f_{\text{grad}}) dV, \quad (1)
 \end{aligned}$$

with the first term describing the GTTE and the bulk free energy density f_{bulk} can be approximated by a Landau polynomial,

$$\begin{aligned} f_{\text{bulk}} = & A_1 \sum_{i=1,2,3} P_i^2 + A_{111} \sum_{i=1,2,3} P_i^4 \\ & + \frac{A_{12}}{2} \sum_{i,j=1,2,3; i \neq j} (P_i P_j)^2 \\ & + A_{111} \sum_{i=1,2,3} P_i^6 + A_{112} \sum_{i,j=1,2,3; i \neq j} P_i^2 P_j^4 \\ & + A_{123} (P_1^2 P_2^2 P_3^2), \end{aligned} \quad (2)$$

where A_1 , A_{111} , A_{12} , A_{111} , A_{112} , and A_{123} are the dielectric stiffness and higher-order stiffness coefficients. The effect of point defects on the transition temperature is described through the temperature dependence of the leading term coefficient, i.e., $A_1 = A_1^0(T - T_c)$, $T_c = T_c^{00} - bc$, where c is the average defect concentration, T_c^{00} is the transition temperature at $c = 0$, and b is a constant.

The second term describes the LFE where

$$f_{\text{couple}} = - \int d^3x \sum_i P_i(\mathbf{x}) \cdot \boldsymbol{\varphi}_{\text{loc}}(\mathbf{x}), \quad (3)$$

and $\boldsymbol{\varphi}_{\text{loc}}(\mathbf{x})$ is a random vector field (local polarization field) created by the point defects.^{10,11,17} $\boldsymbol{\varphi}_{\text{loc}}(\mathbf{x})$ is assumed to have a zero mean and short-range spatial correlations.¹⁷ The last integral in Eq. (1) includes the long-range elastic and electrostatic interaction energies and the short-range exchange interaction energy. The elastic energy density f_{elas} is described as $f_{\text{elas}} = \frac{1}{2} C_{ijkl} e_{ij} e_{kl} = \frac{1}{2} C_{ijkl} (\varepsilon_{ij} - \varepsilon_{ij}^0) (\varepsilon_{kl} - \varepsilon_{kl}^0)$, where e_{ij} , ε_{ij} , and ε_{ij}^0 denote the elastic strain, total strain, and spontaneous strain, respectively. The spontaneous strain in our simulation is given by $\varepsilon_{ij}^0 = Q_{ijkl} P_k P_l$, where Q_{ijkl} is the electrostrictive coefficient of a single crystal. The elastic energy can be calculated by using the phase field microelasticity theory²³ based on Green's function solutions. The contribution of domain walls to the total free energy, f_{grad} , is introduced through the spatial gradient of the polarization field $f_{\text{grad}} = \frac{1}{2} G_{11} \sum_{i=1}^3 \Delta P_i$, where G_{11} is the gradient energy coefficient and $\Delta P_i = \sum_j \frac{\partial^2 P_i}{\partial x_j^2}$. The electrostatic energy density f_{elec} includes the dipole-dipole interaction energy density f_{dipole} , the depolarization energy density f_{depol} , and the energy density caused by applied electric field f_{appl} . The total electrostatic energy can then be described as a combination of the above-mentioned energies $f_{\text{elect}} = f_{\text{dipole}} + f_{\text{depol}} + f_{\text{appl}}$. The long-range dipole-dipole interaction energy density is given by $f_{\text{dipole}} = -\frac{1}{2} E_i P_i$, where E_i denotes the inhomogeneous electric field due to dipole-dipole interactions. The depolarization energy density is given by $f_{\text{depol}} = -\frac{1}{2} E_{i,\text{depol}} \overline{P}_i$, where $E_{i,\text{depol}}$ describes the average depolarization field caused by surface charges and \overline{P}_i denotes the spatial average of the i th component of polarization. The electrostatic energy due to an external electric field $E_{i,\text{appl}}$ is given by $f_{\text{appl}} = -\frac{1}{2} E_{i,\text{appl}} \overline{P}_i$.

The temporal evolution of the spontaneous polarization field can be obtained by solving the time-dependent Ginzburg-Landau equation $\frac{dP_i(\mathbf{x},t)}{dt} = -M \frac{\delta F}{\delta P_i(\mathbf{x},t)}$, $i = 1,2,3$, where M is

the kinetic coefficient and t is time. The following parameters used previously^{21,22} are adopted in the current paper: Landau expansion coefficients $A_1^0 = 0.0035$, $A_{11} = -6.697$, $A_{12} = 3.23$, $A_{111} = 82.94$, $A_{112} = 447.0$, and $A_{123} = 691.0$, elastic constants $C_{11} = 1780.0$, $C_{12} = 964.0$, and $C_{44} = 1220.0$, and electrostrictive coefficients $Q_{11} = 0.10$, $Q_{12} = -0.034$, and $Q_{44} = 0.029$ (all in dimensionless units). The domain-wall energy for 90° domain walls is assumed to be $\sim 0.1 \text{ J m}^{-2}$,²⁴ which yields a length scale of $l_0 \sim 2.0 \text{ nm}$ (where l_0 is the numerical grid size). The simulations are carried out in two dimensions (2D). A periodic boundary is used, and the simulation cell size is 256×256 (i.e., $\sim 0.5 \mu\text{m} \times 0.5 \mu\text{m}$). The time scale can be calculated through $t = \frac{P^2 \times l_0}{M \times \gamma} = 2.4 \times 10^{-13} \text{ s}$,²⁵ where $M = 4 \times 10^4 \text{ C}^2 \text{ J}^{-1} \text{ ms}^{-1}$ (Ref. 26) is the domain wall mobility, $P = 0.757 \text{ C/m}^2$ is the spontaneous polarization, and γ is the domain-wall energy. In our simulations, a step-cooling process is employed, and at each temperature, the system is equilibrated for 50 000 time steps ($\sim 10^{-8} \text{ s}$).

III. RESULTS

A. Phase diagram of polar states in doped ferroelectrics

The simulation results obtained upon cooling from a paraelectric state at different defect concentrations ($c = 0.0$ – 0.4) are shown in Fig. 1. The insets show the diffuse scattering patterns (i.e., the Fourier transform of $|P_i(\mathbf{x})|^2$). In the cases of $c = 0.0$ and $c = 0.02$, the system transforms sharply into typical ferroelectric domain structures with long-range spatial correlations (as indicated by the diffuse scattering patterns) and well-defined 90° and 180° domain walls. When the defect concentration increases to $c = 0.05$ – 0.1 , small polar nanodomains start to appear at high temperatures, which is similar to the precursory tweed structure observed in ferroelastic systems.¹¹ Such a precursory state transforms into a normal ferroelectric domain structure upon further cooling but with much smaller domain sizes. The diffuse scattering patterns show weak spatial alignment. When the defect concentration exceeds a critical value $c > 0.1$, the nanosized polar domains become randomly distributed in space and no longer transform into the normal ferroelectric domain structures. The diffuse scattering pattern does not show clear spatial alignment. This is consistent with the experimental observations.^{4,26,27} Direct TEM observations of $(\text{Pb}_{1-x}\text{La}_x)\text{TiO}_3$ ²⁷ have shown different polar domain states at different defect concentrations. In $(\text{Pb}_{1-x}\text{La}_x)\text{TiO}_3$, long-range-ordered micron-sized tetragonal domain structures can be seen for $x = 0.2$, whereas, only fine domainlike striations are found for $x = 0.23$. For $x = 0.25$, only polar nanodomain contrast can be observed, typical of a glassy polar state seen in relaxor ferroelectrics (Fig. 6 in Ref. 27).

To study whether the randomly distributed nanoscale polar domains shown in Fig. 1 are glassy, ZFC/FC simulations are performed, and the typical result obtained at $c = 0.3$ is shown in Fig. 2(a). The FC curve shows a monotonic change in polarization with temperature, whereas, the ZFC curve shows a clear peak at T_f . The ZFC and FC curves begin to deviate from each other at T_B [the branching temperature indicated in the inset of Fig. 2(a)], which means that the system begins to lose its ergodicity and static nanodomains begin to appear at

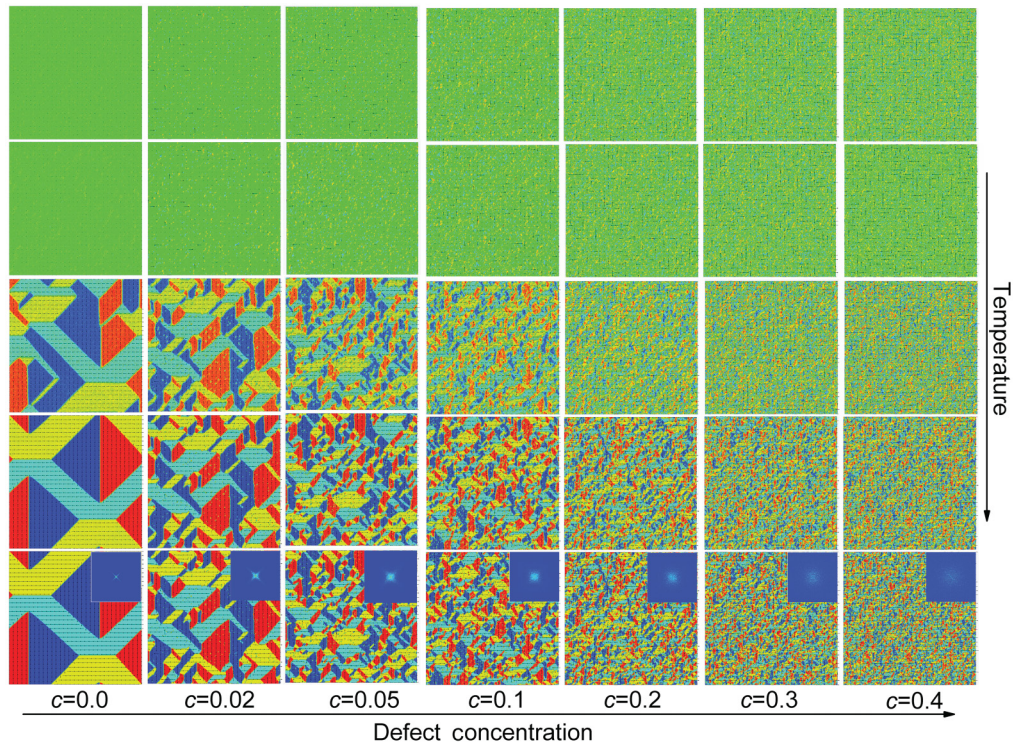


FIG. 1. (Color online) Polar domain structures with different defect concentrations at different temperatures. Different colors describe different polarization domains, and arrows indicate the polarization directions. The system size is $\sim 0.5 \mu\text{m} \times 0.5 \mu\text{m}$. The insets in the bottom row are the diffuse scattering of the corresponding domain structures.

this temperature. At higher temperatures, the system is at a paraelectric state (polar liquid) with ergodic properties. When the temperature is below T_B but above T_f , there exist both dynamic and static nanosized polarization domains. When the temperature is below T_f , the polar nanodomains are completely

frozen, and the system transforms into a ferroelectric-glass state.

It should be noted that the ZFC peak position is defined as a glass-freezing temperature T_f ,²⁸ where the system loses its ergodicity completely. More interestingly, our simulated

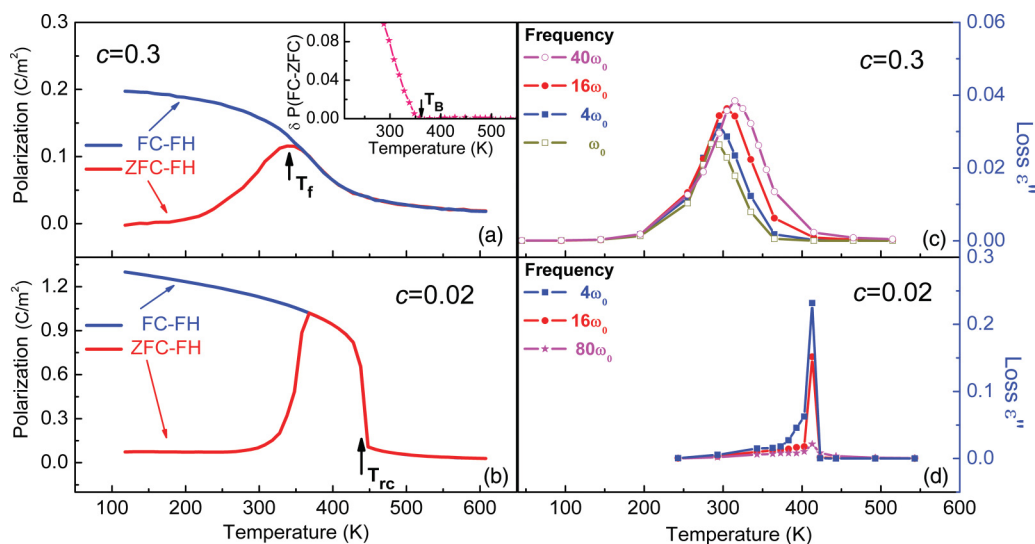


FIG. 2. (Color online) (a) ZFC/FC curves for a system with a defect concentration of $c = 0.3$, where T_f indicates the ZFC peak temperature and T_B indicates the branching temperature. The deviation in the FC curve from the ZFC curve around the branching point is plotted in the inset. (b) ZFC/FC curves for a system with a defect concentration of $c = 0.02$. (c) and (d) Loss dielectric permittivity obtained at different frequencies for the two systems.

ZFC/FC curves shown in Fig. 2 exhibit a striking similarity to the ZFC/FC curves obtained experimentally for the relaxor in the $(\text{Pb}_{1-x}\text{La}_x)(\text{Zr}_{1-y}\text{Ti}_y)\text{O}_3$ (PLZT) system,⁷ strain glass,²⁹ and cluster-spin glass.³⁰ In contrast, the ZFC/FC curves of a normal ferroelectric phase transition (at $c = 0.02$) [Fig. 2(b)] are found to be associated with a jump at the reverse ferroelectric transition temperature T_{rc} with large polarization, followed by a separation at low temperatures. Furthermore, the obvious frequency dependence of the dielectric loss for the relaxor transition ($c = 0.3$) shown in Fig. 2(c) is a typical signature of a relaxor observed in the experiments.¹⁻⁶ For comparison, the frequency independence of the dielectric loss obtained for the normal ferroelectric transition ($c = 0.02$) is shown in Fig. 2(d). The dielectric loss ε'' is calculated through applying an ac field cycle [with different periods (the reciprocal of frequency)] with a small electric field at different temperatures.

The nanosize polar domains shown in Fig. 1, the ZFC/FC curves, and the frequency dependence of dielectric loss shown in Fig. 2 have confirmed the existence of ferroelectric-glass transition at high defect concentrations. Figure 3(a) shows the heat capacity (C_p) calculated from the simulation results¹¹ as well as the ZFC/FC curves obtained for different defect concentrations. The peak temperature of the C_p curve obtained upon cooling is defined as the normal ferroelectric transition temperature T_c at low defect concentrations, whereas, the peak temperatures of the ZFC curves are defined as the ferroelectric-

glass-freezing temperature T_f at high defect concentrations.¹¹ The branching temperatures T_B on the ZFC/FC curves indicate the start of the appearance of static, nonergodic polar nanodomains and are defined as the precursory polar states start temperatures. These transition temperatures, determined from Fig. 3(a), are plotted in Fig. 3(b) for different defect concentrations, which yield a polar state phase diagram that describes the relationships among all the polar states in a doped ferroelectric system. For example, it captures the normal ferroelectric transition, the ferroelectric-glass transition, and the appearance of a high-temperature precursory state.^{26,31} This calculated phase diagram shows striking common features with the experimentally determined phase diagram of PLZT.⁵

B. Properties associated with normal ferroelectrics and relaxor transitions

Figure 4 shows the comparisons of different properties associated with a normal ferroelectric transition ($c = 0.02$) to those associated with a ferroelectric-glass transition ($c = 0.3$). The heat-capacity curves show a sharp peak at the ferroelectric transition [Fig. 4(a)] and a diffuse hump at the relaxor transition [Fig. 4(b)]. Figures 4(c) and 4(d) show the remnant polarization vs temperature curves for the two transitions. Comparing with the sharp change in polarization at the reverse transition temperature T_{rc} upon heating obtained from the normal ferroelectric transition [Fig. 4(c)], the relaxor transition shows a gradual vanishing of polarization. Figures 4(e)–4(h) show the related polarization-electric (P-E) field curves and the electrostrictive strain-electrical field curves obtained for the two systems at three different temperatures: $T = 273, 323,$ and 393 K. The normal ferroelectric system exhibits a hysteresis loop that has a large remnant polarization P_R , whereas, the relaxor exhibits a slim hysteresis loop with a small remnant polarization. The inset in Fig. 4(f) shows the temperature dependence of χ_3 , the third-order dielectric susceptibility, which is calculated through fitting the P-E curves by $P = \chi_1 E + \chi_3 E^3 \dots$. The calculation shows an obvious peak, which agrees with the experimental observation.³² Furthermore, the frequency dependence of dielectric permittivity $\varepsilon'(\omega)$ and loss dielectric permittivity $\varepsilon''(\omega)$ for the relaxor ($c = 0.3$) are shown in Figs. 5(a) and 5(b), which are calculated through applying an ac field cycle with a small electric field at different temperatures. The solid lines are predictions from the Cole-Cole equations,

$$\varepsilon' = \varepsilon_\infty + (\varepsilon_s - \varepsilon_\infty) \frac{1 + (\omega\tau_0)^{1-\alpha} \sin(\pi\alpha/2)}{1 + 2(\omega\tau_0)^{1-\alpha} \sin(\pi\alpha/2) + (\omega\tau_0)^{2(1-\alpha)}}, \quad (4)$$

$$\varepsilon'' = (\varepsilon_s - \varepsilon_\infty) \frac{(\omega\tau_0)^{1-\alpha} \cos(\pi\alpha/2)}{1 + 2(\omega\tau_0)^{1-\alpha} \sin(\pi\alpha/2) + (\omega\tau_0)^{2(1-\alpha)}}, \quad (5)$$

where ε_∞ and ε_s are the dielectric permittivity at infinite frequencies and the static dielectric permittivity, respectively, ω is the frequency, α is the distribution degree of relaxation time, and τ_0 is the relaxation time. As shown in Fig. 5(b), the relaxation time $\tau = 2\pi/\omega$ increases, and the distribution of relaxation times broadens upon cooling. The inset in Fig. 5(b) shows clearly broadening of the distribution of relaxation

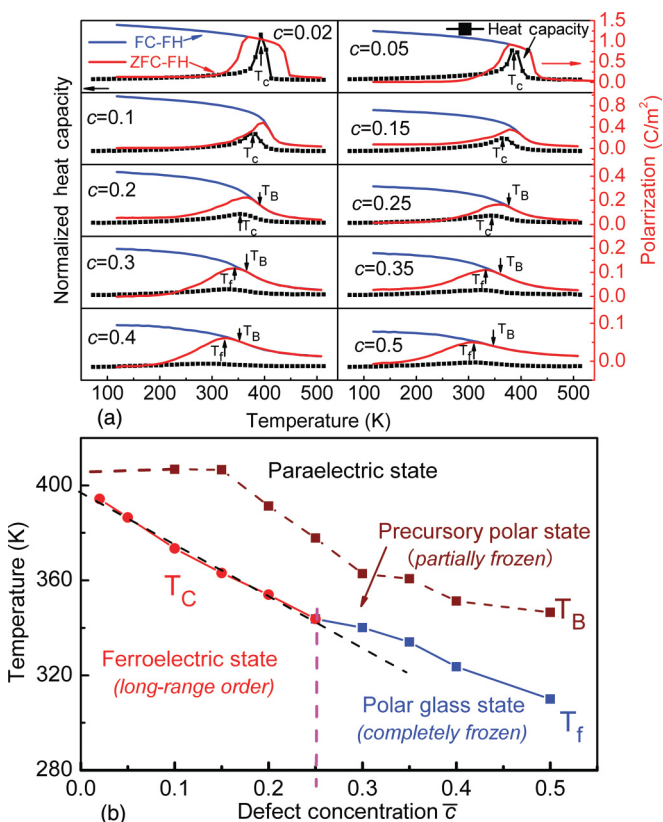


FIG. 3. (Color online) (a) Transition temperatures determined from the heat-capacity and ZFC/FC curves. (b) Corresponding polar state phase diagram constructed using the transition temperatures indicated in (a).

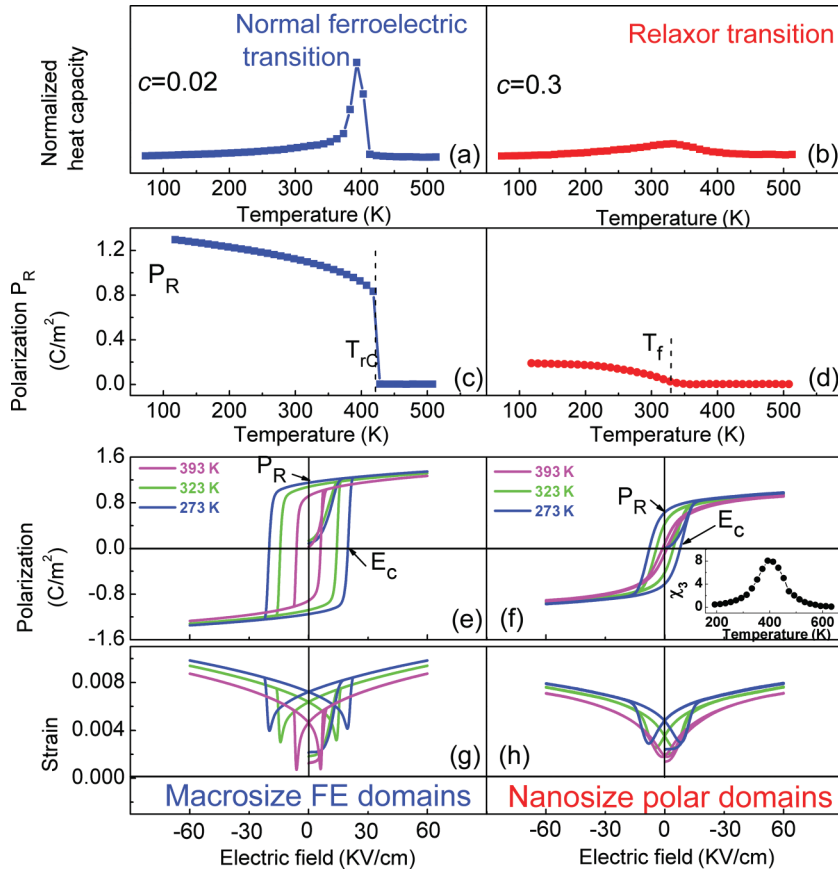


FIG. 4. (Color online) Physical properties associated with the normal ferroelectric transition ($c = 0.02$) and relaxor transition ($c = 0.3$): (a) and (b) heat capacity, (c) and (d) remnant polarization (P_R) change upon heating, (e) and (f) hysteresis loop, and (g) and (h) electrostrictive strain vs electric field at different temperatures. The inset in (f) describes the temperature dependence of the third-order dielectric susceptibility χ_3 .

time ($\tau_l - \tau_0 - \tau_h$) and slowing down of the kinetic process (increase in τ_0) upon cooling. Here, τ_0 corresponds to the peak position in $\epsilon''(\omega)$, and τ_l and τ_h correspond to $\epsilon'' = 0.001$ at the low- and high-frequency ranges, respectively. Even though the actual calculation time spans from 10^{-2} to 10^{-8} , the calculated data follow the Cole-Cole equations well and, hence, a rather wide relaxation time distribution (e.g., 10^{-8} – 10^2 s at 303 K) has been obtained as shown in the inset of Fig. 5(b). These

calculations agree well with experimental observations.³³ The frequency dispersion in our simulation comes from the size distribution of the nanopolar domains. Domains of different sizes have different response times to the external fields, leading to the broadening distribution of relaxation time. It should be pointed out that other types of relaxation, such as space charge at lower frequencies or electrons at higher frequencies are not considered in these calculations.

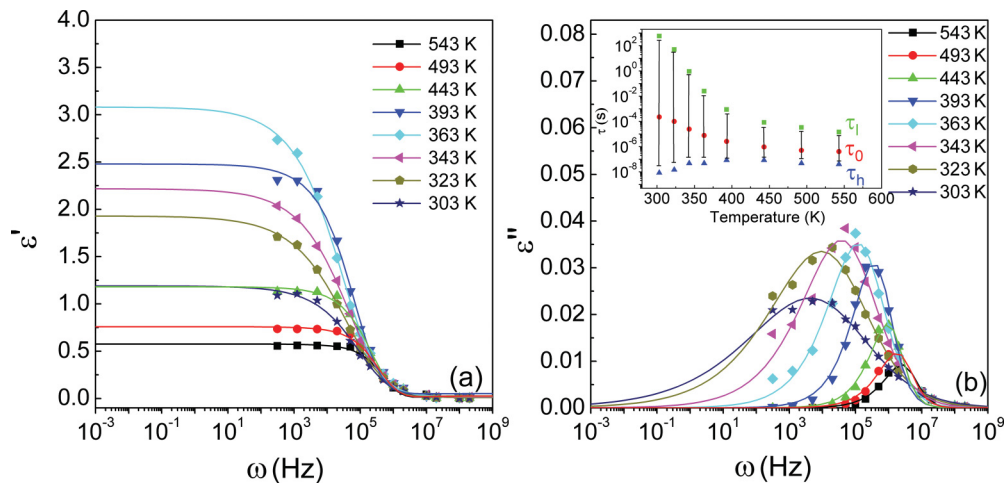


FIG. 5. (Color online) The frequency dependence of (a) dielectric permittivity $\epsilon'(\omega)$ and (b) loss dielectric permittivity $\epsilon''(\omega)$ for relaxor ($c = 0.3$) at different temperatures. Symbols show the calculated results, and solid lines show predictions from the Cole-Cole equations. The inset in (b) describes the relaxation time distribution $\tau(1/\omega)$ according to $\epsilon''(\omega)$. τ_0 shows the relaxation time at peak position in the $\epsilon''(\omega)$ curves, while τ_l and τ_h show the relaxation time with $\epsilon'' = 0.001$ at a low-frequency range and a high-frequency range, respectively.

IV. DISCUSSION

A. Effect of point defects on the formation of relaxor

By coupling the LFE with the GTTE, the phase field simulations have reproduced all the unique properties associated with the normal ferroelectric and relaxor transitions, upon which, a complete phase diagram of all the polar states in a generic-doped ferroelectric system has been established. The GTTE lowers the global stability of the ferroelectric phase and, thus, results in a decrease in the normal ferroelectric phase transition temperature T_c . The LFE breaks the symmetry of the Landau free energy^{10,11} with respect to polarization and prefers certain polarizations at randomly distributed defect locations, which hinder the formation of long-range correlated ferroelectric domains. At low defect concentrations, the resistance to long-range correlation in ferroelectric domain structures from the point defects is not strong enough to prevent the system from transforming from a polar liquid to a polar crystal upon cooling. Because of the LFE, however, static polar nanodomains (precursory state, partially nonergodic) appear at T_B , which is above the normal ferroelectric transition temperature T_c . When the point defect concentration is high enough, the randomly distributed local polarization fields created by the point defects prevent the formation of long-range-ordered polar states (polar crystals), and the system is frozen into a ferroelectric polar glass with randomly distributed static nanoscale polar domains. Note that because of the displacive nature, a normal ferroelectric transition takes place at a time scale of 10^{-12} – 10^{-9} s in micrometer-size systems,³⁴ which is much faster than any experimentally accessible cooling rate. Thus, a normal ferroelectric material (i.e., with low defect concentrations) cannot transform into a glassy state (i.e., relaxor) even under a very fast cooling rate or quenching. It is the point defects that “freeze” the polar configuration into a glass state in doped ferroelectrics. Thus, doped ferroelectric materials that have strong random local fields (electric or stress) present, such as heterovalent-doped $(\text{Bi}_{2/3x}\text{Sr}_{1-x})\text{TiO}_3$,

$(\text{Pb}_{1-x}\text{La}_{2/3x})(\text{Zr}_y\text{Ti}_{1-y})\text{O}_3$ (PLZT), and equivalently doped $\text{BaSn}_x\text{Ti}_{1-x}\text{O}_3$ and $\text{BaZr}_x\text{Ti}_{1-x}\text{O}_3$ are promising candidates for relaxor ferroelectrics.

Note that our model is formulated for *A*-site substitution systems, such as $(\text{Bi}_{2/3x}\text{Sr}_{1-x})\text{TiO}_3$ and $(\text{Pb}_{1-x}\text{La}_{2/3x})(\text{Zr}_y\text{Ti}_{1-y})\text{O}_3$ that produce local polarization because of the heterovalent-doped point defects. In these systems, x must be above a critical value for the ferroelectric-glass properties to appear. However, this model can also shed light on the nonequivalent *B*-site substitution and equivalent *B*-site substitution systems. The local polarization field in the former and the local strain/stress fields in the latter caused by dopants should play an important role in the formation of ferroelectric glasses.

B. Ruggedness of a free energy landscape in doped ferroelectrics

The wide relaxation time as shown in Fig. 5 has proved the glassy characteristics of the relaxor in our simulation. To describe the physical origin of this important dynamic property, the ruggedness of the free energy landscape with increasing defect concentration is calculated, and the result is shown in Fig. 6. We plot the total free energy landscape [i.e., Eq. (1): local Landau free energy + gradient energy + electrostatic interaction energy + elastic interaction energy] of doped ferroelectric systems with different defect concentrations. The system size is 256×256 (~ 500 nm) (single crystal), and a free surface condition (i.e., without depolarization energy caused by surface charges) is used. There exist two degenerated polarization states P_x ([100] direction) and P_y ([010] direction) in this 2D system, determined by the Landau polynomial. For the sake of simplicity, we use the average polarization of the whole system to represent the “space configuration.” The *X* axis in Fig. 6 describes the value of average polarization at the [100] direction, i.e., \bar{P}_x and the *Y* axis describes the calculated total free energy with different space configurations. In these

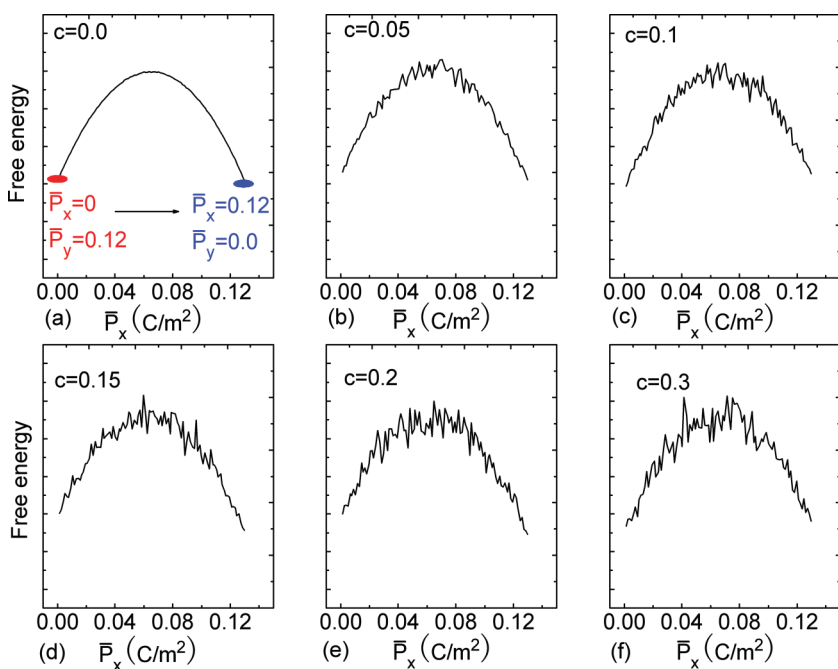


FIG. 6. (Color online) The total free energy landscape of doped ferroelectric systems having defect concentrations from 0.0 to 0.3. The system size is 256×256 . The *x* axis describes the “configuration space.” In these plots, we use the average polarization in the [100] direction \bar{P}_x to represent the configuration space, e.g., the left side ($\bar{P}_x = 0$ and $\bar{P}_y = 0.12$) describes the single domain structure with all [010] polarizations, and the right side ($\bar{P}_x = 0.12$ and $\bar{P}_y = 0$) describes the single domain structure with all [100] polarizations. All the states in between are polydomain states with different average polarizations \bar{P}_x .

calculations, the ground states are the single domain states, corresponding to a single domain of [100] polarization on the left and a single domain of [010] polarization on the right, respectively, in Fig. 6. All the states in between are polydomain states with different average polarizations \bar{P}_x . Figures 6(a)–6(f) show the free energy landscape change with increasing defect concentrations from $c = 0.0$ to $c = 0.3$. It is readily seen that the ruggedness of the free energy landscape increases with increasing defect concentration. At low defect concentrations ($c < 0.15$), there just exists a single large barrier between the two different single domain states, and the free energy shows a smooth variation with the space configuration. Therefore, it is relatively easy for the system to go to either of these two ground states (i.e., the single domain states). However, at high defect concentrations ($c > 0.15$), the doped defects alter the free energy landscape significantly, and there are a lot of local minima and local barriers between the two ground states. In this case, it is difficult for the system to evolve into the ground states (much longer relaxation time). So, with the increase in defect concentration, the local barriers become higher and higher, and correspondingly, the relaxation times \bar{P}_x become longer and longer.

V. CONCLUSIONS

With the consideration of global transition temperature effect and local field effect, phase field simulations have reproduced both normal ferroelectric transition and ferroelectric-glass transition. All the characteristics associated with a

ferroelectric polar glass state predicted by the simulations agree well with experimental observations, including wide relaxation time, “diffuse” transition, temperature dependence of third-order dielectric susceptibility, nonergodicity, frequency dependence of dielectric loss, and domain switching. Based on these results, a complete ferroelectric-glass crossover phase diagram including all the polar states [paraelectric state, normal ferroelectric state, precursory polar state, and polar glass state (randomly distributed nanosized ferroelectric domains)] in a doped ferroelectric system is established, which describes the relationships among these polar states in the temperature-defect concentration space. Furthermore, the simulations predict the unique dynamical nature of the relaxor, i.e., relaxation that extends over an extremely wide range of time. The physical origin could be attributed to the defect-induced ruggedness of the free energy landscape.

ACKNOWLEDGMENTS

The work was supported by the National Basic Research Program of China (Grants No. 2012CB619402 and No. 2010CB631003), the National Natural Science Foundation of China (Grants No. 51101118, No. 51071117, No. 50720145101, and No. 50771079), and the 111 Project of China (Project No. B06025) (D. Wang), the US Natural Science Foundation Grant No. DMR-1008349 (Y. Wang), and the Japan KAKENHI (X. B. Ren).

*Corresponding author: wang.363@osu.edu

†ren.xiaobing@nims.go.jp

¹A. A. Bokov and Z. G. Ye, *J. Mater. Sci.* **41**, 31 (2006).

²M. I. Marqués and C. Aragó, *Phys. Rev. B* **81**, 064114 (2010).

³G. A. Samara, *J. Phys.: Condens. Matter* **15**, R367 (2003).

⁴D. Fu, H. Taniguchi, M. Itoh, S. Y. Koshihara, N. Yamamoto, and S. Mori, *Phys. Rev. Lett.* **103**, 207601 (2009).

⁵L. E. Cross, *Piezoelectricity Evolution and Future of a Technology*, edited by W. Heywang, K. Lubitz, and W. Wersing, Springer Series in Materials Science Vol. 114 (Springer, Berlin, 2008), p. 131.

⁶B. E. Vugmeister and M. D. Glinchuk, *Rev. Mod. Phys.* **62**, 993 (1990).

⁷D. Viehland, J. F. Li, S. J. Jang, L. E. Cross, and M. Wuttig, *Phys. Rev. B* **46**, 8013 (1992).

⁸K. Uchino, *Piezoelectric Actuators and Ultrasonic Motors* (Kluwer Academic, Boston, 1996).

⁹Z. Kutnjak, J. Petzelt, and R. Blinc, *Nature (London)* **441**, 956 (2006).

¹⁰A. P. Levanyuk and A. Sigov, *Defects and Structural Phase Transitions* (Gordon and Breach Science, New York, 1988).

¹¹D. Wang, Y. Wang, Z. Zhang, and X. Ren, *Phys. Rev. Lett.* **105**, 205702 (2010).

¹²M. D. Glinchuk and R. Farhi, *J. Phys.: Condens. Matter* **8**, 6985 (1996).

¹³A. A. Bokov, *Ferroelectrics* **190**, 197 (1997).

¹⁴P. N. Timonin, *Ferroelectrics* **199**, 69 (1997).

¹⁵S. Semenovskaya and A. G. Khachatryan, *J. Appl. Phys.* **83**, 5125 (1998).

¹⁶V. Westphal, W. Kleemann, and M. D. Glinchuk, *Phys. Rev. Lett.* **68**, 847 (1992).

¹⁷Y. Imry and S. K. Ma, *Phys. Rev. Lett.* **35**, 1399 (1975).

¹⁸R. Pirc and R. Blinc, *Phys. Rev. B* **60**, 13470 (1999).

¹⁹R. Blinc, J. Dolinšek, A. Gregorovič, B. Zalar, C. Filipič, Z. Kutnjak, A. Levstik, and R. Pirc, *Phys. Rev. Lett.* **83**, 424 (1999).

²⁰E. V. Colla, E. Y. Koroleva, N. M. Okuneva, and S. B. Vakhrushev, *Phys. Rev. Lett.* **74**, 1681 (1995).

²¹Y. L. Li, L. E. Cross, and L. Q. Chen, *J. Appl. Phys.* **98**, 064101 (2005).

²²Y. L. Li and L. Q. Chen, *Appl. Phys. Lett.* **88**, 072905 (2006).

²³A. G. Khachatryan, *Theory of Structural Transformations in Solids* (Wiley, New York, 1983).

²⁴S. Choudhury, Y. L. Li *et al.*, *Acta Mater.* **53**, 5313 (2005).

²⁵J. Hlinka, *Ferroelectrics* **349**, 49 (2007).

²⁶D. Viehland, M.-C. Kim, Z. Xu, and J.-F. Li, *Appl. Phys. Lett.* **67**, 2471 (1995).

²⁷X. Dai, Z. Xu, and D. Viehland, *J. Appl. Phys.* **79**, 1021 (1996).

²⁸J. A. Mydosh, *Spin Glasses* (Taylor & Francis, London, 1993).

²⁹D. Wang, Z. Zhang *et al.*, *Acta Mater.* **58**, 6206 (2010).

³⁰N. Gayathri, A. K. Raychaudhuri, S. K. Tiwary, R. Gundakaram, A. Arulraj, and C. N. R. Rao, *Phys. Rev. B* **56**, 1345 (1997).

³¹G. Burns and F. H. Dacol, *Phys. Rev. B* **28**, 2527 (1983).

³²A. Levstik, Z. Kutnjak, C. Filipič, and R. Pirc, *Phys. Rev. B* **57**, 11204 (1998).

³³V. Bovtun, S. Veljko, S. Kamba, J. Petzelt *et al.*, *J. Eur. Ceram. Soc.* **26**, 2867 (2006).

³⁴J. Hlinka, V. Stepkova, P. Marton, I. Rychetsky *et al.*, *Phase Transitions* **84**, 738 (2011).